Journal of Sound and Vibration 325 (2009) 798–815

Contents lists available at ScienceDirect

Journal of Sound and Vibration

journal homepage: www.elsevier.com/locate/jsvi

On the modeling of vibration transmission over a spatially curved cable with casing

Miha Otrin, Miha Boltežar *

University of Ljubljana, Faculty of Mechanical Engineering, Aškerčeva 6, 1000 Ljubljana, SI, Slovenia

ARTICLE INFO

Article history:
Received 15 August 2008
Received in revised form
14 January 2009
Accepted 31 March 2009
Handling Editor: M.P. Cartmell
Available online 9 May 2009

ABSTRACT

We propose an approach to the vibration modeling of spatially curved steel wires with a casing and a contact between the outer casing and the inner steel wire. For the mathematical model of the steel wire and the outer casing, the Euler–Bernoulli beam theory with no axial pre-load is used, and for the discretisation, finite elements are used. The excitation of the steel wire and the outer casing is in the form of random kinematic excitation. For the energy dissipation the proportional viscous damping model and the structural damping model are used. The damping parameters are identified from the Nyquist diagram and from the continuous wavelet transform. For the identification of the frequency dependence of the dynamic modulus of elasticity a method is proposed that uses the measured natural frequencies and the experimentally determined natural modes. The contact between the steel wire and the outer casing is modelled using the penalty method with the friction in a tangential direction. We show that higher values of the friction coefficient have a significant influence on lowering the level of vibration transmission. The model also predicts that the dynamic modulus of the elasticity of a steel wire does not have a major influence on the level of vibration transmission, which was also validated by experiment. On the basis of an experimental validation the model of a steel wire with an outer casing proved to be suitable for the prediction of the vibration transmission.

1. Introduction

The cable is a well-known structural element in engineering. The main purpose of cables is to bear relatively large axial forces in comparison to bending forces, e.g., cable-stayed bridges and lifting cranes. In recent years the automotive industry has had a requirement to model vibration transmission over spatially curved cables with a casing and with no axial pre-load. The studied cable with its casing is part of the gear-shift mechanism and can, under some circumstances, produce high-level noise in the passenger cabin. From this perspective, knowing the dynamic behaviour of a cable–casing system is very important. In the studied case the cable with a casing represents a structure made of an inner steel cable (later denoted as the cable), and an outer casing (later denoted as the casing). The casing has a similar structure to the cable (helically sweeping steel wires, see Fig. 2), so the investigation of the cable also applies to the investigation of the casing. The radial gap between the cable and the casing causes mechanical contacts between them along their lengths, especially when the load is applied in a lateral direction to the cable's axis.

* Corresponding author. Tel.: +386 1 4771 608; fax: +386 1 2518 567.
E-mail address: miha.boltezar@fs.uni-lj.si (M. Boltežar).

0022-460X/$ - see front matter © 2009 Elsevier Ltd. All rights reserved.
doi:10.1016/j.jsv.2009.03.045

In the past a number of investigations into the dynamic behaviour of a cable have been carried out with a consideration of a non-zero axial pre-load. In the literature two different modeling approaches for the static and dynamic analyses of cables can be found. The first approach is more oriented to a detailed analysis of the cable strand, with the emphasis on modeling each strand of wire separately. This offers an insight into different inter-wire motions in the strand and a possible fatigue investigation of each wire. Using this approach, Costello [1] proposed a mathematical model for the static and dynamic analyses of a cable strand, with the assumption that the centre wire is of sufficient size to prevent the outer wires from touching each other. Nawrocki and Labrosse [2] presented a finite-element model of a straight wire-rope strand. They considered either a pure axial load or an axial load combined with a bending load. Their model has proved to be reliable when compared with experimental data for every possible inter-wire motion. The second approach is more oriented to modeling the cable as a homogeneous circular cross-section [4–7]. Barbieri et al. [3,4] proposed a finite-element model for the derivation of the eigenvalues and the eigenvectors for all situations of mechanical load (except where only a bending load is acting on the cable) and sample length. The model was validated with an experiment and proved to be reliable. It was also shown that the damping ratio increases with the increasing length of the specimen. Gattulli et al. [5] proposed a nonlinear, analytical and finite-element model for the analysis of a cable's dynamics. They studied the stability of the cable's oscillations in the resonant regions under harmonic loading. They showed that the unstable regions are due to the modal interactions.

Another significant aspect of cable dynamics is the consideration of the energy dissipation. Many damping models have been developed over the years [8–11,13], but so far none of them can be used to describe the damping characteristics of an arbitrary structure. The reason is in the material and the shape dependence of the energy dissipation. Consequently, the damping model is different for every studied structure, depending on the most influential damping mechanism. Because of their simplicity, two damping models, i.e., viscous and structural, are the most widely used models for the characterisation of energy loss in structural dynamics [14,15].

The influence of the gap and, consequently, the contact that arises between the cable and the casing has a significant influence on the casing–cable dynamics. Various authors addressed a similar problem when analysing, for example, windmill dynamics [16,17] and drillstring dynamics [18,19], where the flexible rotating beam is interacting with a flat rigid surface. What is very significant for the given examples is the high relative velocities in the stator–rotor interaction and a single contact point. The similarity with our study is in the geometries of the two bodies in contact, i.e., they are circular. The authors addressed the rotor–stator interaction, but only one contact at a time. In contrast, we studied bodies that are both deformable and with simultaneous radial contacts along the length of the cable with a casing.

A detailed numerical and experimental study of the dynamics of a spatially curved cable with no axial pre-load was presented in Ref. [20]. In Ref. [21] a numerical simulation of the transmission of vibrations over a casing–cable with a frictionless contact in the radial direction is introduced.

This paper presents a new approach to modeling and testing a spatially curved cable–casing dynamical system where the gap between the cable and the casing has a significant influence. The main emphasis is on the modeling of the contact geometry and the contact forces, where both the cable and the casing have their own excitations. The results of the analysis make it possible to choose the geometrical and material parameters in such a way that the dynamic transmission and the influence of the contact are minimised. It is organised as follows. In Section 2 the physical and mathematical models with two possible damping models (viscous and structural) are shown to characterise the vibrations of the spatially curved casing with no axial pre-load. The mathematical model is based on the Euler–Bernoulli theory. The contact model is also addressed. In Section 3 the Rayleigh coefficients, the loss factor, and the dynamic modulus of elasticity are identified. In Section 4 the validation of the lateral force's transmission over the spatially curved casing with the kinematic support movement and the interaction of a casing–cable system is described. The influences of the geometrical and material parameters on the dynamics of the cable with a casing are also shown. In Section 5 we draw some conclusions.

2. Theoretical background

A casing–cable is made of two separate structures: the cable and the casing. An essential characteristic of a mathematical model for the dynamic analyses of both structures is the absence of an axial load. It is shown in Ref. [4] that a cable can, in general, be modelled as a beam structure with the consideration of an axially acting load. Our studies in Ref. [20] showed that the usage of the Euler–Bernoulli beam theory for the mathematical model of a spatially curved cable with no axial pre-load gives a good insight into its dynamic behaviour. In this paper we consider the dynamic behaviour of a spatially curved casing with no axial pre-load and its interaction with the cable that was studied in Ref. [20].

The Euler–Bernoulli beam equation is used to model the lateral vibrations of the casing, and for the numerical computation we used finite elements. The emphasis is placed on the linear damping, i.e., proportional viscous damping in terms of the Rayleigh coefficients and structural damping in terms of the complex modulus of elasticity. The linear assumption for the strain (displacement) and the damping comes mainly from the low-level excitation regime that influences the casing–cable during real operation in a car. These assumptions suggest the use of a relatively simple mathematical model for the analysis of fairly complicated casing–cable dynamics, where contacts can arise and which also results in a shorter computational time of the response. The physical model of the casing is shown in Fig. 1.

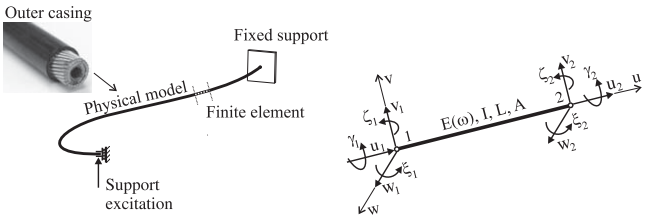

Fig. 1. The physical model for the spatially curved casing and its finite element.

In the finite-element formulation the following assumptions were made: geometrical linearity for small displacements, the level of excitation is low, the plane section remains planar after deformations, the material of the cable is homogeneous and isotropic, and the displacements and rotations are uncoupled. If geometrical linearity and low-level excitation are not assumed, nonlinearities in the stiffness and the damping are introduced, which would result in a different modeling principle. Beginning from the differential equation for the lateral vibrations

$$\frac{\partial^2}{\partial x^2}\bar{E}(\omega)I\frac{\partial^2 w(x,t)}{\partial x^2}+c\frac{\partial w(x,t)}{\partial t}+\rho A\frac{\partial^2 w(x,t)}{\partial t^2}=f(x,t), \tag{1}$$

the torsional vibrations

$$\frac{\partial}{\partial x}\left(\bar{G}(\omega)J\frac{\partial\theta(x,t)}{\partial x}\right)-c_t\frac{\partial\theta(x,t)}{\partial t}+m_T(x,t)=I_0\frac{\partial^2\theta(x,t)}{\partial t^2}, \tag{2}$$

and the longitudinal vibrations

$$\frac{\partial}{\partial x}\left(\bar{E}(\omega)A\frac{\partial u(x,t)}{\partial x}\right)-c_l\frac{\partial u(x,t)}{\partial t}+f_l(x,t)=\rho A\frac{\partial^2 u(x,t)}{\partial t^2}, \tag{3}$$

the mass $\mathbf{M}_e$ matrix, the damping $\mathbf{C}_e$ matrix, the stiffness $\mathbf{K}_e$ matrix, and the vector of external load $\mathbf{F}_e$ of the finite element are formalised as follows:

$$\mathbf{M}_e=\int_V \mathbf{N}^{\mathrm{T}}\rho\mathbf{N}\,\mathrm{d}V, \tag{4}$$

$$\mathbf{C}_e=\int_V \mathbf{N}^{\mathrm{T}}c\mathbf{N}\,\mathrm{d}V, \tag{5}$$

$$\mathbf{K}_e=\int_V \mathbf{B}^{\mathrm{T}}\mathbf{D}\mathbf{B}\,\mathrm{d}V, \tag{6}$$

$$\mathbf{F}_e=\int_V \mathbf{N}^{\mathrm{T}}\mathbf{f}\,\mathrm{d}V, \tag{7}$$

where $\mathbf{B}$ is the strain–displacement matrix, $\mathbf{D}$ is the stress–strain matrix of the material of volume $\mathrm{d}V$, $\mathbf{N}$ is the interpolation function matrix of the finite element, ρ is the mass density, and i is the i-th finite element. In Eqs. (1)–(3) the $f(x,t)$ is the external force per unit length, A is the area of the cross-section, $w(x,t)$ is the lateral displacement at distance x and at time t, I is the second area moment, c, c_t, and c_l are the viscous-damping coefficients, J is the second area polar moment of the cross-section, $\theta(x,t)$ is the angle of twist at a distance x and at time t, I_0 is the moment of inertia per unit length, m_T is the applied twisting moment per unit length, $u(x,t)$ is the longitudinal displacement at a distance x and at time t, and $f_l(x,t)$ is the longitudinal external force. $\bar{E}(\omega)$ and $\bar{G}$ are the complex modulus of elasticity and the complex shear modulus, respectively.

In the numerical finite element two separate damping models are considered. For the viscously damped model we assume the damping matrix $\mathbf{C}\neq\mathbf{0}$ and the real value of the complex modulus of elasticity, and for the structurally damped model we assume $\mathbf{C}=\mathbf{0}$ and the complex modulus of elasticity in the form $\bar{E}(\omega)=E_d(\omega)+\mathrm{i}E_l(\omega)=E_d(\omega)(1+\mathrm{i}\eta(\omega))$, where $E_l(\omega)$ is the loss modulus, $E_d(\omega)$ is the dynamic modulus, $\eta(\omega)$ is the loss factor, and $\mathrm{i}=\sqrt{-1}$.

Bearing in mind Fig. 1, the nodal displacements are

$$\mathbf{q}=\{u_1\ \ v_1\ \ w_1\ \ \gamma_1\ \ \zeta_1\ \ \xi_1\ \ u_2\ \ v_2\ \ w_2\ \ \gamma_2\ \ \zeta_2\ \ \xi_2\}^{\mathrm{T}}, \tag{8}$$

and the displacement function $\hat{\mathbf{q}}$ of the finite element is

$$\hat{\mathbf{q}}=\mathbf{N}\mathbf{q}, \tag{9}$$

where $\mathbf{N}$ represents the interpolation functions of the finite element. In the case of lateral vibrations of the cable, the third-order Hermitian polynomials are used, and for the torsional and longitudinal vibrations the second-order polynomials are used. Because of the spatially curved casing, the finite elements were transformed from the local to the global coordinate

system through the direction-cosine-matrix (rotational matrix). The more detailed steps for the definition of the transformation matrix are given in Ref. [20].

The dynamic equation for the viscous damping model is shown in Eq. (10), and for the structural damping model in Eq. (11),

$$\mathbf{M}\ddot{\mathbf{q}}_v(t) + \mathbf{C}\dot{\mathbf{q}}_v(t) + \mathbf{K}\mathbf{q}_v(t) = \mathbf{F}_v\, e^{i\omega t}, \tag{10}$$

$$\mathbf{M}\ddot{\mathbf{q}}_s(t) + (1 + i\eta)\mathbf{K}\mathbf{q}_s(t) = \mathbf{F}_s\, e^{i\omega t}, \tag{11}$$

where **M**, **K**, and **C** are the mass, stiffness, and viscous damping matrices of the system of finite elements and **F** is the vector of the nodal forces of the finite elements. Index v denotes the mathematical model with the viscous damping model and s with the structural damping model. For the purposes of validation the transfer function in terms of the apparent mass (TRFAM) was used [20]. TRFAM, Eq. (12), is defined in the frequency domain and gives the vibration's transmissibility when the input disturbance is in the form of the support excitation at one end of the casing and the output disturbance is in the form of the support force at the other end of the casing, Fig. 1.

$$TRFAM(\omega) = \frac{\mathbf{f}_p}{\mathbf{x}_p}. \tag{12}$$

For the purposes of computing the TRFAM, it is useful to rewrite Eqs. (10) and (11) as partially uncoupled equations with partitioning to the known and unknown node displacements and rotations with regard to the partitioned vectors

$$\mathbf{q} = [\mathbf{x}_{v,s}\ \ \mathbf{x}_p]^T \quad \text{and} \quad \mathbf{F} = [\mathbf{f}_{v,s}\ \ \mathbf{f}_p]^T, \tag{13}$$

where index p denotes the supported nodes. With Eq. (13) it has to be emphasised that for the validation of the casing's dynamics the steady-state solution was computed and for the casing–cable interaction the time solution was computed according to the Newmark scheme algorithm. The feature of the steady-state solutions is the ability to use both viscous and structural damping models in accordance with a solution of the form $\mathbf{q}(t) = \mathbf{x}\, e^{i(\omega t+\varphi)}$.

2.1. Casing–cable interaction

When analysing the cable with a casing as a coupled structure, an evaluation of the contact between the casing and the cable is needed. We considered multiple contacts with friction, with an additional identification of a stick–slip contact phase. The layout of the addressed problem is shown in Fig. 2.

For the normal contact direction the normal forces of the casing–cable system were computed using the penalty method [22]. The reason for using this method is its compatibility with the finite-element model.

By defining the casing boundary with $\varphi(\beta^2)$ and the cable boundary with $\varphi(\beta^1)$, the two bodies come into contact when the node points $\mathbf{x}^2$ and $\mathbf{x}^1$ on each casing–cable system find the condition in time $\varphi(\mathbf{x}^1, t) = \varphi(\mathbf{x}^2, t)$. The graphical formation is shown in Fig. 3.

With the penalty method the stiffness and the damping contact forces are defined with the direction of the contact normal. For an arbitrary position of the casing and the cable the contact normal vector **n** was defined in the direction normal to the node. The normal vector also defines the penetration vector $\mathbf{g}_n$, Fig. 4. Furthermore, if we define the cable as the master body and the casing as the slave body, the normal direction $\mathbf{n}^1$ is conditioned by the cable nodes and the cable boundary. The distance between the cable nodes and the crossing of the normal vector with the casing boundary defines the penetration vector $\mathbf{g}_n$. It follows that the penetration vector is not conditioned by the node-to-node contact but by the node-to-boundary contact, Fig. 4, where the contact point at the casing boundary is denoted with $\bar{\mathbf{x}}^2$.

The penetration function is set with the relation

$$\mathbf{g}_n = \begin{cases} (\bar{\mathbf{x}}^2 - \mathbf{x}^1)\mathbf{n}^1 & \text{when } (\bar{\mathbf{x}}^2 - \mathbf{x}^1)\mathbf{n}^1 < 0, \\ 0 & \text{when } (\bar{\mathbf{x}}^2 - \mathbf{x}^1)\mathbf{n}^1 \geqslant 0. \end{cases} \tag{14}$$

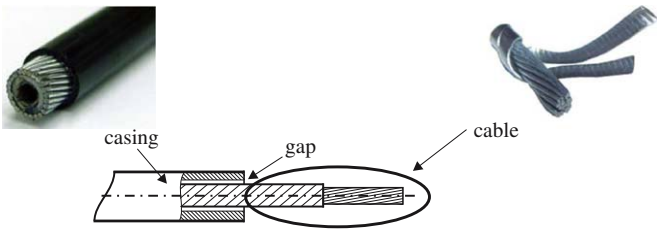

Fig. 2. The layout of the cable with casing.

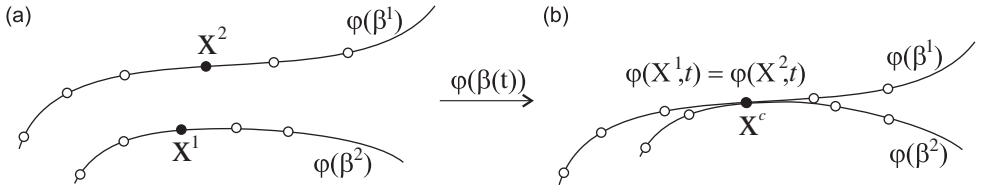

Fig. 3. The casing–cable contact definition.

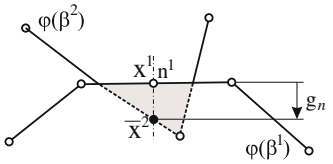

Fig. 4. The definition of the contact normal vector.

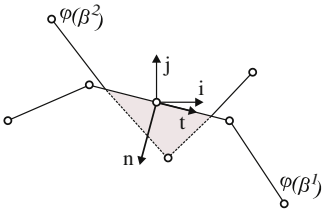

Fig. 5. The notations of the global and contact unit vectors.

By knowing the penetration vector $\mathbf{g}_n$, the stiffness contact forces can be defined with

$$\mathbf{f}_n^c = \begin{cases} \varphi(\beta^1) \rightarrow k_n^p \cdot \mathbf{g}_n, \\ \varphi(\beta^2) \rightarrow -k_n^p \cdot \mathbf{g}_n, \end{cases} \tag{15}$$

where k_n^p is the stiffness parameter. For a consistent contact model there must be no adhesive forces in the contact-restitution phase. This problem can be solved numerically with the condition

$$\mathbf{d}_n^c = \begin{cases} \mathbf{v}_n^{\mathrm{rel}} \cdot c_n^p, & 0 < t \leqslant t^k, \\ 0, & t^k < t \leqslant t^r, \end{cases} \tag{16}$$

where $\mathbf{d}_n^c$ is the damping contact force, c_n^p is the damping contact coefficient, and $\mathbf{v}_n^{\mathrm{rel}}$ is the relative velocity of the casing–cable system. Here, t^k is the end-of-compression time during the contact phase t. The final contact forces can be rewritten as

$$\mathbf{c}_n = k_n^p \mathbf{g}_n + c_n^p \mathbf{v}_n^{\mathrm{rel}}. \tag{17}$$

Bearing in mind the spatially curved casing–cable system, the friction force vector results from (i) the current casing–cable position, (ii) the contact normal force, and (iii) the tangential relative velocity of the casing–cable system. As the contact normal force is time dependent during the contact phase, so too is the friction force, and to compute the friction force the Coulomb friction law was used. The Coulomb law is the simplest form of defining the friction force so in its general form it does not account for the slip–stick motion between the two bodies. In the literature [23–27] many different approaches have been found for addressing the stick–slip motions of the 1DOF system. The approach we used is based on the observation of the tangential relative velocity of each contact point (possible simultaneous contact). When the relative velocity holds the condition $-\nu_m < \nu_{\mathrm{rel}} < \nu_m$, where ν_{rel} is the tangential relative velocity and $\pm\nu_m$ is the upper/lower relative velocity limit, the stick phase is introduced. Later, the stick force for every contact point was computed from the casing–cable dynamic system. The detailed procedure is as follows. Let us assume we are analysing a dynamic system of finite elements in one plane with the dynamic equation

$$\mathbf{M}\ddot{\mathbf{q}} + \mathbf{C}\dot{\mathbf{q}} + \mathbf{K}\mathbf{q} = \mathbf{f}. \tag{18}$$

Looking at Fig. 5 the global unit vectors **i**, **j** and the contact unit vectors **t**, **n** are introduced. Here **t** and **n** correspond to the tangential and normal directions, respectively.

Let the degrees of freedom of the dynamic system be partitioned to the contact and non-contact points in the global coordinate system according to

$$\mathbf{q} = [\mathbf{q}_i^g \;\; \mathbf{q}_c^g]^{\mathrm{T}}, \tag{19}$$

where the index g represents the global coordinate system, index i the non-contact points, and index c the contact points. If we address the matrices **M**, **C**, and **K** with the general notation **A**, we can rewrite the partition matrix as

$$\begin{bmatrix} \mathbf{A}_{ii} & \mathbf{A}_{ci} \\ \mathbf{A}_{ic} & \mathbf{A}_{cc} \end{bmatrix} \cdot \begin{bmatrix} \mathbf{q}_i^g \\ \mathbf{q}_c^g \end{bmatrix} = \begin{bmatrix} \mathbf{f}_i^g \\ \mathbf{f}_c^g \end{bmatrix} \tag{20}$$

from which follows Eq. (21),

$$\mathbf{A}_{ic}\mathbf{q}_i^g + \mathbf{A}_{cc}\mathbf{q}_c^g = \mathbf{f}_c^g. \tag{21}$$

The vector $\mathbf{f}_c^g$ is the contact force vector in the global coordinate system (unit vector **i**, **j**). If the contact transformation matrix $\mathbf{T}_c$ is introduced, this transforms the contact global coordinate system to the contact local coordinate system (unit vector **t**, **n**)

$$\mathbf{q}_c^g = \mathbf{T}_c\mathbf{q}_c^l, \tag{22}$$

and Eq. (21) can be rewritten as

$$\mathbf{A}_{ic}\mathbf{q}_i^g + \mathbf{A}_{cc}\mathbf{T}_c\mathbf{q}_c^l = \mathbf{T}\mathbf{f}_c^l, \tag{23}$$

where $\mathbf{f}_c^l$ is the contact vector for the normal and tangential directions in the contact point. Because the normal contact force is computed with the penalty method, only the tangential contact force needs to be computed for every contact point and for every computed time. Furthermore this force is used as the check-point value for the stick–slip phase, i.e., if the tangential contact force is higher than the current Coulomb force, the slip phase is addressed and vice versa for the stick phase.

2.1.1. The contact-stiffness function

The contact-stiffness function defines the penetration–force relationship. The most commonly used penetration–force relationship is a linear function of the form

$$\mathbf{f}_n^c = k_n^p\mathbf{g}_n. \tag{24}$$

In the cases where k_n is a known parameter Eq. (24) can be used for most problems. In the studied case, the parameter k_n is not known; instead we used the penetration–force relation from the Hertz contact theory [28–32]. In the Hertz contact theory for circular boundaries, the depth of the penetration **g** depends mainly on the radius and the dynamic modulus of elasticity of the bodies in contact. From Ref. [28] we can calculate the depth of the penetration as

$$\mathbf{g} = \left(\frac{15m\mathbf{v}_0^2}{16r^{0.5}E^*}\right)^{2/5}, \tag{25}$$

with the following relations:

$$\frac{1}{m} = \frac{1}{m_1} + \frac{1}{m_2}, \tag{26}$$

$$\frac{1}{r} = \frac{1}{r_1} + \frac{1}{r_2}, \tag{27}$$

$$\frac{1}{E^*} = \frac{1-v_1^2}{E_1} + \frac{1-v_2^2}{E_2}. \tag{28}$$

Here, m_1, m_2 are the masses of the two bodies, r_1, r_2 are the radii of curvature in the contact point of the two bodies, v_1, v_2 are the Poisson's numbers, E_1, E_2 the dynamic moduli of the two bodies in contact, and $\mathbf{v}_0$ is the relative velocity of the bodies in the normal contact direction. In addition, we can write the relation between the depth of the penetration and the stiffness contact force from Ref. [28] as

$$\mathbf{f}_n^c = \tfrac{4}{3}r^{1/2}E^*\mathbf{g}_n^{3/2}. \tag{29}$$

The main advantage of this approach is that we do not need a special identification process to find the stiffness contact parameter, instead we take into account the material and the geometrical characteristics of the bodies in contact.

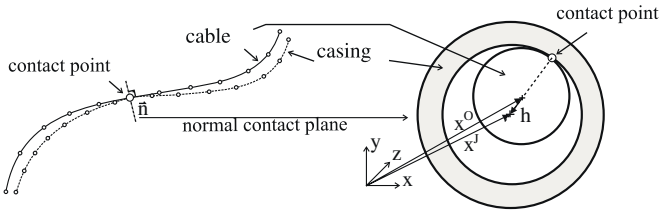

Fig. 6. The contact search along the cable axis.

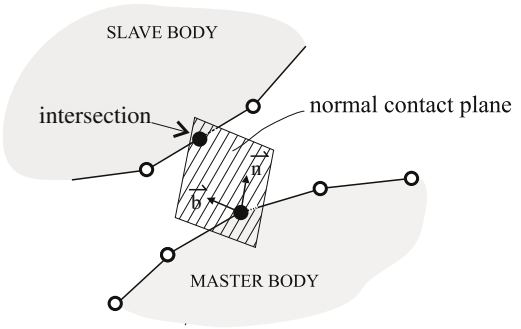

Fig. 7. The intersection between the normal contact plane and the axis of the slave body.

2.1.2. Contact search algorithm

As was shown in Fig. 4, the contact points are found from the node-boundary relations. We chose the cable to be the master body and the casing to be the slave body; therefore, the normal contact planes are defined for every finite-element node of the cable, Fig. 6. If we define the M_j finite elements of the cable, there are $M_j + 1$ potential contact points for the casing–cable system.

Because of the circular cross-section of the cable and the casing the contact condition in the radial direction to the cable axis is defined with

$$h = |\mathbf{x}^J - \mathbf{x}^O| > e \rightarrow \text{contact}, \tag{30}$$

$$h = |\mathbf{x}^J - \mathbf{x}^O| \leqslant e \rightarrow \text{no contact}, \tag{31}$$

where e is the maximum gap between the cable and the casing, $\mathbf{x}^J$ and $\mathbf{x}^O$ are the displacement vectors of the master and the slave body, respectively. It can be shown that the contact point and both centre points of the cross-sections are collinear.

The problem of the contact search can be transformed to a search for the intersection between the normal contact plane at the cable node and the spatially curved axis of the casing, Fig. 7.

The parametric form of the spatially curved master body axis is

$$\mathbf{r}(s) = \mathbf{i}x(s) + \mathbf{j}y(s) + \mathbf{k}z(s), \quad a < s < b, \tag{32}$$

where s is the arbitrary scalar parameter and $\mathbf{i}$, $\mathbf{j}$, $\mathbf{k}$ are the unit vectors for the global coordinate system. From differential geometry theory every point along the curve has its tangent $\mathbf{t}$, normal $\mathbf{n}$, and binormal $\mathbf{b}$ vectors. If the vectors $\mathbf{r}(t)$, $\mathbf{r}'(t)$, and $\mathbf{r}''(t)$ are known, the tangent, normal, and binormal vectors are

$$\mathbf{t} = \frac{\mathbf{r}'(s)}{\|\mathbf{r}'(s)\|}, \tag{33}$$

$$\mathbf{b} = \frac{\mathbf{r}'(s) \times \mathbf{r}''(s)}{\|\mathbf{r}'(s) \times \mathbf{r}''(s)\|}, \tag{34}$$

$$\mathbf{n} = \mathbf{b} \times \mathbf{t}. \tag{35}$$

It follows from Fig. 7 that the normal and binormal vectors form the normal contact plane. The normal contact plane can be further defined as

$$\mathbf{p}_0 + (\mathbf{p}_1 - \mathbf{p}_0)u + (\mathbf{p}_2 - \mathbf{p}_0)v, \quad u, v \in \mathbb{R}, \tag{36}$$

where $\mathbf{p}_k = (x_k, y_k, z_k)$, $k = 0, 1, 2$ are the three non-collinear points that form the normal contact plane, and u and v are the two scalar parameters. Similarly, the parametric form for the line is

$$\mathbf{i}_a + (\mathbf{i}_b - \mathbf{i}_a)l, \quad l \in \mathbb{R}, \tag{37}$$

where $\mathbf{i}_a = (x_a, y_a, z_a)$ and $\mathbf{i}_b = (x_b, y_b, z_b)$ are the points that define the line. From Eqs. (36) and (37) the equation for the intersection is defined as

$$\mathbf{i}_a + (\mathbf{i}_b - \mathbf{i}_a)l = \mathbf{p}_0 + (\mathbf{p}_1 - \mathbf{p}_0)u + (\mathbf{p}_2 - \mathbf{p}_0)v, \tag{38}$$

or in matrix form

$$\begin{bmatrix} l \\ u \\ v \end{bmatrix} = \begin{bmatrix} x_a - x_b & x_1 - x_0 & x_2 - x_0 \\ y_a - y_b & y_1 - y_0 & y_2 - y_0 \\ z_a - z_b & z_1 - z_0 & z_2 - z_0 \end{bmatrix}^{-1} \begin{bmatrix} x_a - x_0 \\ y_a - y_0 \\ z_a - z_0 \end{bmatrix}. \tag{39}$$

The solution of l, u, and v gives the exact intersection point from where the penetration vector can be computed.

3. Parameter identification

Usually, the researcher does not have all the information about the material characteristics of the studied structure, so for a proper validation of the mathematical model, the parameters need to be identified. In this study the main unknown parameters are the dynamic modulus of elasticity and the damping parameters for the viscous and structural damping models of the casing.

3.1. Identification of the dynamic modulus of elasticity

The used identification process for the frequency dependence of the dynamic modulus of elasticity in Fig. 8 was introduced in Ref. [20]. The computed values of the natural frequencies were adapted to the measured ones. The iteration process continued until the differences between the computed and the measured values of the natural frequencies were half of the frequency resolution in the measured TRFAM, which was 0.25 Hz.

For the cable the frequency-dependent dynamic modulus of elasticity was presented in Ref. [20], and for the casing it is shown in Fig. 9. The presented frequency-dependent modulus of elasticity of the casing was used in the validation process of the mathematical model.

3.2. Identification of the damping parameters

For the used damping models, the damping matrix **C** in Eq. (10), and the loss factor η in Eq. (11) have to be identified.

3.2.1. Identification of the damping matrix

The viscous damping is modelled in the form of proportional (equivalent) Rayleigh damping, Eq. (40), where the Rayleigh coefficients α and β have to be identified. Let us reflect that the emphasis of this paper is on the cable–casing interaction, so the use of a simple damping model is justified. Our studies also showed that a slight change in the damping

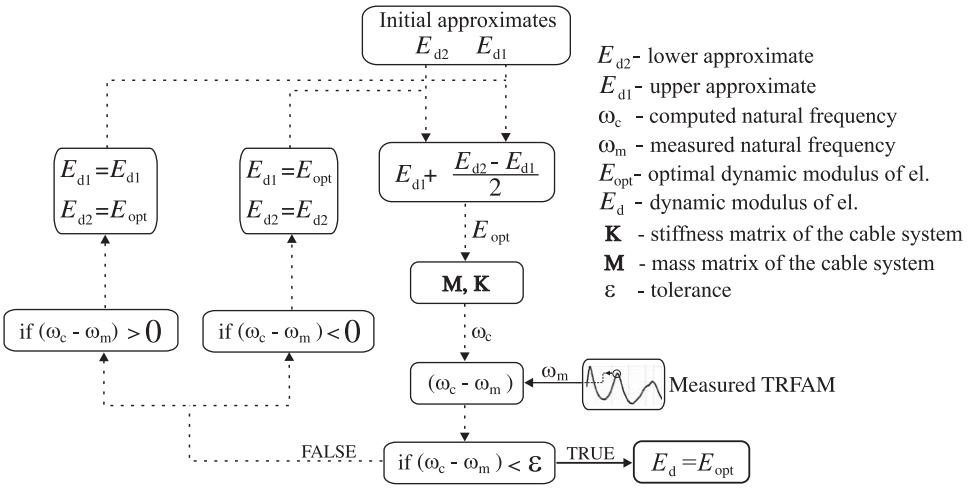

Fig. 8. The adaptive process (- - -) for the identification of the frequency dependence of the dynamic modulus of elasticity E_d.

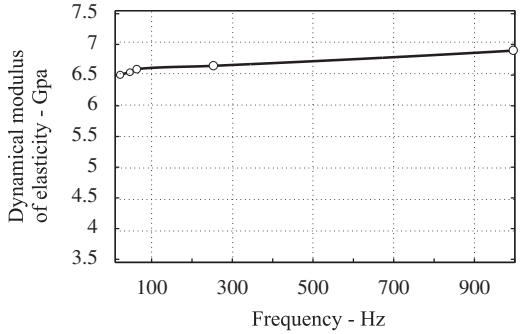

Fig. 9. The approximated curve of the frequency-dependent modulus of elasticity of the casing (—) over the measured natural frequencies (○).

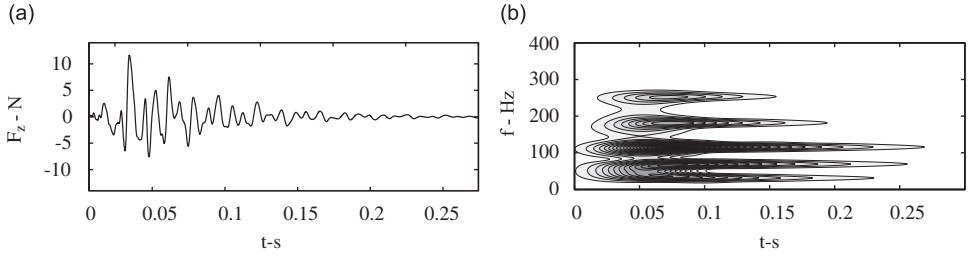

Fig. 10. The impulse time response and its wavelet transform at the clamped support.

forces has no significant influence on the system's (cable–casing with a gap) time response.

$$\mathbf{C} = \alpha\mathbf{M} + \beta\mathbf{K}. \tag{40}$$

It can be shown from the orthogonality principle [33] that the relation between the i-th damping ratio ζ and the i-th natural frequency ω_i can be written in the form

$$\zeta_i = \frac{\alpha}{2\omega_i} + \frac{\beta\omega_i}{2}. \tag{41}$$

Rewriting Eq. (41) in the matrix form

$$\begin{bmatrix} \tilde{\zeta}_1 \\ \tilde{\zeta}_2 \\ \vdots \\ \tilde{\zeta}_m \end{bmatrix} = \begin{bmatrix} \frac{1}{2\tilde{\omega}_1} & \frac{\tilde{\omega}_1}{2} \\ \frac{1}{2\tilde{\omega}_2} & \frac{\tilde{\omega}_2}{2} \\ \vdots & \vdots \\ \frac{1}{2\tilde{\omega}_m} & \frac{\tilde{\omega}_n}{2} \end{bmatrix} \begin{bmatrix} \alpha \\ \beta \end{bmatrix}, \tag{42}$$

the parameters α and β can be estimated from the identified natural frequencies $\tilde{\omega}_m$ and damping ratios $\tilde{\zeta}_m$. With the simplified matrix notation of Eq. (42)

$$\mathscr{Z} = \mathscr{A} \cdot \mathscr{C}, \tag{43}$$

the α and β can be solved with the pseudo-inverse process:

$$\mathscr{C} = (\mathscr{A}^T\mathscr{A})^{-1}\mathscr{A}^T\mathscr{Z} = \mathscr{A}^+\mathscr{Z}. \tag{44}$$

Identification of the damping ratio: For the identification of the damping ratio the wavelet-based method was used; this method is well explained in Ref. [34]. The main idea behind the identification process is finding the ridge of the wavelet transform of the measured impulse response in the time domain (in our study it was at the clamped support). The example of the identification is shown on the basis of the numerical example of the casing. The impulse response and its wavelet transform can be seen from Fig. 10.

The ridges at the natural frequencies are shown in Fig. 11. The $\ln(W(s_g, u))$ is the logarithmic wavelet transform of the wavelet ridge at the scale s_g. The identified damping ratios are given in Table 1.

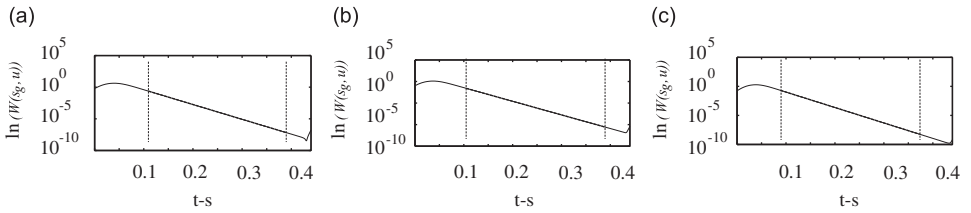

Fig. 11. The ridges of the wavelet transform at the natural frequencies f_r: (a) $f_r = 115.84$ Hz; (b) $f_r = 181.97$ Hz; and (c) $f_r = 254.14$ Hz.

Table 1
The identified damping ratios and loss factors for the numerical example.

Natural frequency (Hz)	115.8	182.0	254.1
Damping ratio	0.0359	0.0263	0.0216
Loss factor	0.0764	0.046	0.0448
$\zeta = \eta/2$, [36]	0.0382	0.0230	0.0224

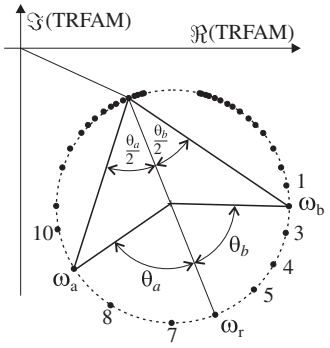

Fig. 12. The Nyquist plot of the TRFAM for the identification of the loss factor.

3.2.2. *Identification of the loss factor*

Many different methods, e.g., the standing-wave method and the non-resonant method, have been developed to identify the complex modulus and the loss factor. In our study the loss factor was estimated from the Nyquist plot of the measured TRFAM (Fig. 12). For linear systems the Nyquist plot (for cases of receptance, mobility, and accelerance) should, in the resonant region, take the approximate shape of a circle [14,35]. From the theoretical point of view any possible deviation from a circle, for example, an ellipse, can be caused by structural nonlinearities in the stiffness or damping terms, which we did not observe. The process is schematically presented in Fig. 12.

From Refs. [14,35] Eq. (45) is derived for the exact identification of the loss factor η:

$$\eta_r = \frac{\omega_a^2 - \omega_b^2}{\omega_r^2} \frac{1}{\tan(\theta_a) + \tan(\theta_b)}, \tag{45}$$

where ω_a and ω_b are the lower and upper boundary frequencies, and θ_a and θ_a are the angles from Fig. 11. It is useful to first approximate the circle to the measured points in the Nyquist diagram. For that we used the nonlinear curve-fitting technique (nonlinear least-squares method) that has proven to give better results in comparison to the linear curve fitting. Studies have shown that it is best to first compute the loss-factor plane for every combination of the frequency points on the fitted circle [35]. A more precise loss-factor can later be derived from the diagonal ridge of the loss-factor plane, as will be shown in following example.

The same example as in Section 3.2.1 was made on the basis of a Nyquist plot. In Fig. 13 the identification results are presented. In Fig. 13(a–c) the Nyquist plots with the fitted circle to the numerically derived TRFA are shown, in Fig. 13(d–f) the loss-factor plane is shown, and in Fig. 13(g–i) the ridge on the main diagonal of the loss-factor plane is shown. The identified loss factors are given in Table 1.

3.3. *Comparison of the identified damping parameters from two different identification process*

Henwood [36] has shown that a loss factor of less than 0.4 can be approximated with the known damping ratios of the viscous damping model by $\eta \approx 2\zeta$. Bearing in mind this relation we can compare the two identification processes, i.e., the

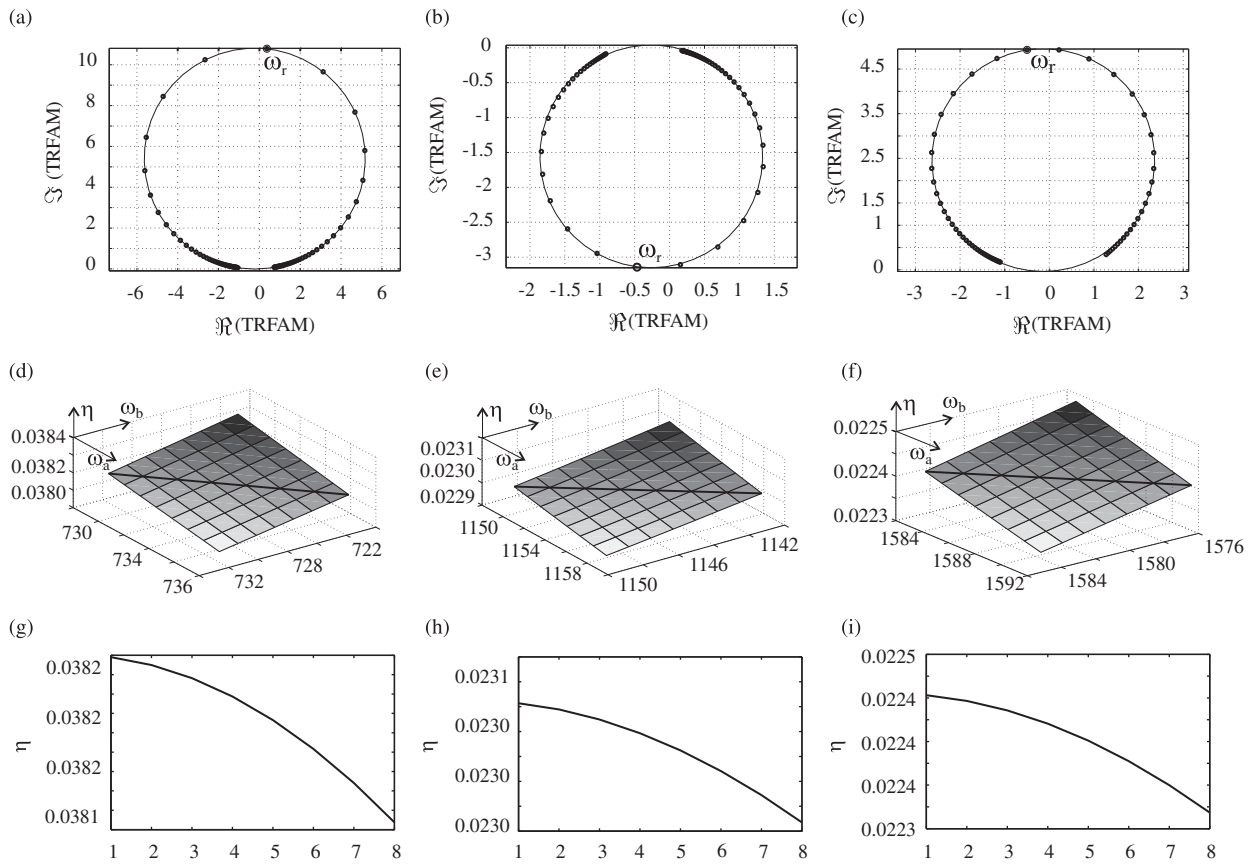

Fig. 13. The identification of the loss factor; (a–c) Nyquist plot, (d–f) the loss-factor plane, (g–i) the ridge of the main diagonal of the loss-factor plane: (a) $f_r = 115.8$ Hz; (b) $f_r = 182.0$ Hz; (c) $f_r = 254.1$ Hz; (d) $f_r = 115.8$ Hz; (e) $f_r = 182.0$ Hz; (f) $f_r = 254.1$ Hz; (g) $f_r = 115.8$ Hz; (h) $f_r = 182.0$ Hz; and (i) $f_r = 254.1$ Hz.

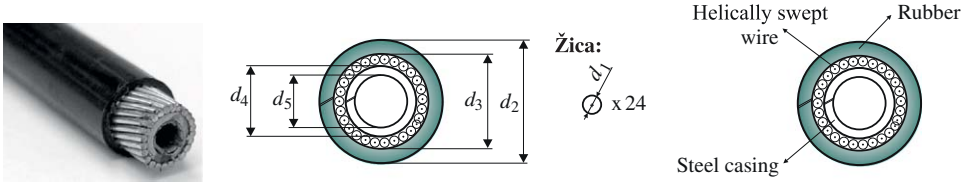

Fig. 14. The cross-section of the casing.

wavelet-based identification based on the time-domain signal and the identification from the Nyquist plot based on the frequency-domain signal.

Table 1 shows the identified damping parameters for the numerical example derived in Sections 3.2.1 and 3.2.2.

4. Experimental case study

4.1. Dynamic validation of the casing

The suitability of the mathematical model used for the casing–cable interaction needs to be first validated for the casing itself. With that we are taking account of the fact that the vibration transmission of the cable was validated in Ref. [20]. The casing cross-section is shown in Fig. 14 and the geometrical parameters are shown in Table 2, where I_{op} is the second area moment, ρ_{op} is the averaged density, d_1 is the diameter of the curved wire, d_2 is the outer diameter of the casing, d_3 is the inner diameter of the rubber casing, d_4 is the outer diameter of the steel casing, d_5 is the inner diameter of the steel casing, φ_{op} is the angle of the helical sweep of the wires, and s_{op} is the number of wires.

Table 2
The geometrical properties of the casing.

I_{op} (m^4)	ρ_{op} (kg/m^3)	d_1 (m)	d_2 (m)	d_3 (m)	d_4 (m)	d_5 (m)	φ_{op} (deg)	s_{op} (–)
2.7261×10^{-10}	4850	0.00078	0.0095	0.0077	0.0059	0.004	75	24

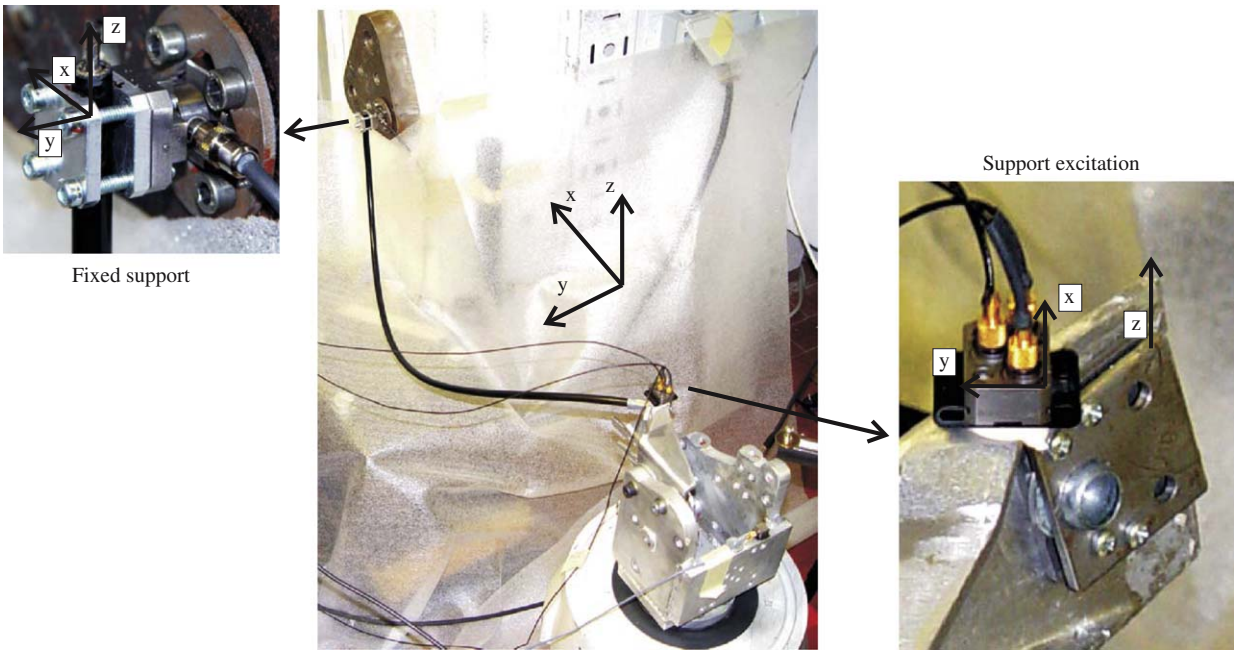

Fig. 15. The experimental set-up for the casing validation.

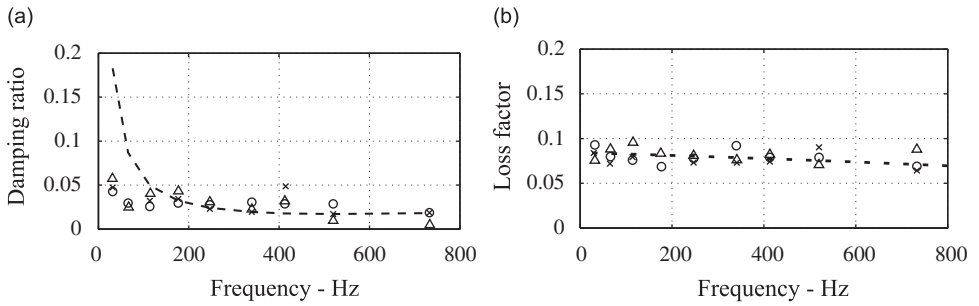

Fig. 16. The identified damping parameters for the (○) x, (△) y, (×) z directions of the measured TRFAM: (a) damping ratio and (b) loss factor.

The casing's dynamics was validated with the experiment. The excitation of the casing was achieved with the electrodynamic shaker at the one supported end of the casing, while the support force was measured at the other casing end. One end of the casing was excited with a broadband noise signal in the frequency range from 10 to 1000 Hz, with the RMS value of the excitation signal equal to 5 ms^{-2}. The experimental set-up is shown in Fig. 15. What is important to realise with the experimental set-up is that we are validating the spatially curved casing, and that the excitation amplitude is low for an assumption of model linearity. We used a special fixing cube on the side of the shaker, which allows the excitation in each of three x, y, z directions. The length of the casing was 850 mm.

The identified damping ratios for the casing are shown in Fig. 16(a). The dashed line incorporates the Rayleigh coefficients $\alpha = 11.1$ and $\beta = 4.23 \times 10^{-5}$ that are used in the mathematical model with viscous damping. The identified loss factors are shown in Fig. 16(b), where the approximated dashed line was used in the mathematical model with structural damping. Again, we must point out that the damping ratios were identified with the wavelet-based technique,

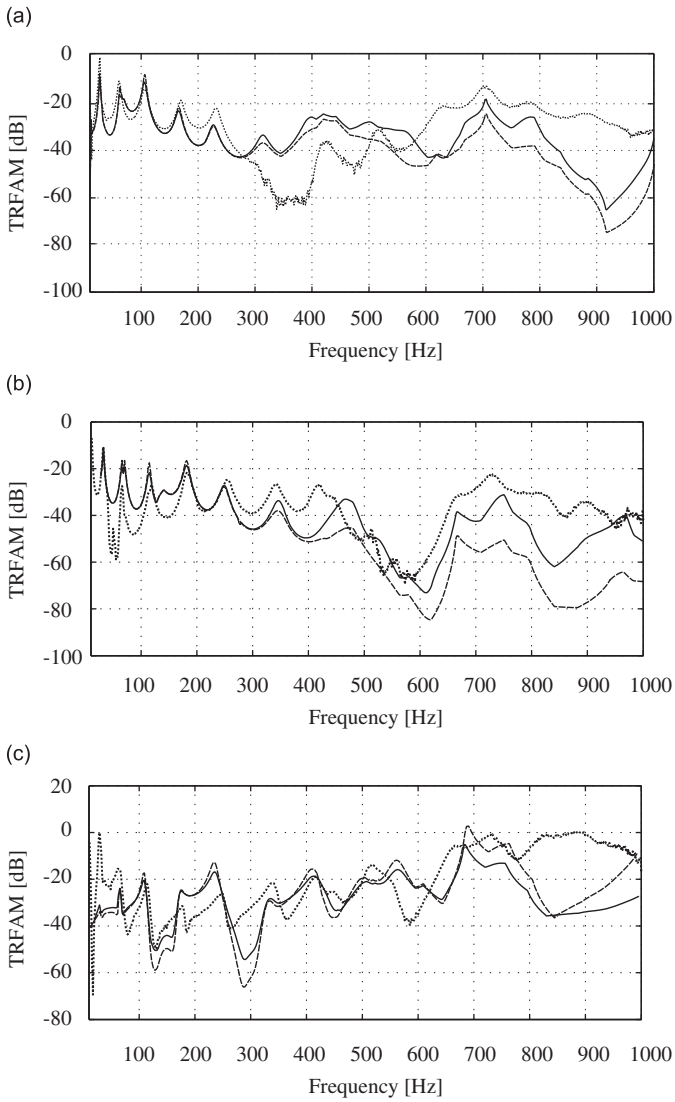

Fig. 17. The TRFAM of the spatially curved casing. Measured (...); computed: structural damping (—), viscous damping (- - -): (a) direction x; (b) direction y; and (c) direction z.

and the loss-factor came from the Nyquist plot. The validation on the basis of the TRFAM is shown for all three analysed directions in Fig. 17(a–c). The casing was modelled with 35 finite elements. The time response computed with this number of elements shows a sufficiently small difference compared to the time response using a larger number of finite elements (e.g., 200). For an appropriate number of finite elements the mean-square-error estimation (in our case $MSE<3$) was used.

4.2. Casing–cable interaction

When the mathematical models for the cable [20] and the casing, Section 4, are properly validated, the casing–cable interaction can then be studied [37]. In the real application the cable with a casing is influenced by the separate support excitation of the cable and the casing. For this purpose we designed an additional support excitation for the cable in its longitudinal direction. The experimental set-up for the validation of the casing–cable interaction is shown in Fig. 18.

The contact parameters used in the numerical analyses are: the stiffness parameter k_n^p is determined from Hertz contact theory, the damping parameter is $c_n^p = 100\,\mathrm{kg/s}$, and the coefficient of friction is $\eta = 0.15$. It follows from the Hertz theory and from the material parameters of our study, that the stiffness-penetration relationship can be computed, Fig. 19. This relationship was later used in all the numerical simulations.

The longitudinal excitation of the cable from Fig. 18 was 50 Hz with the chosen acceleration amplitude. Our studies have showed that if the cable is not separately excited in the longitudinal direction it has no major influence on the casing–cable dynamics. The noticeable influence of the casing–cable interaction can be seen when the cable has its own excitation,

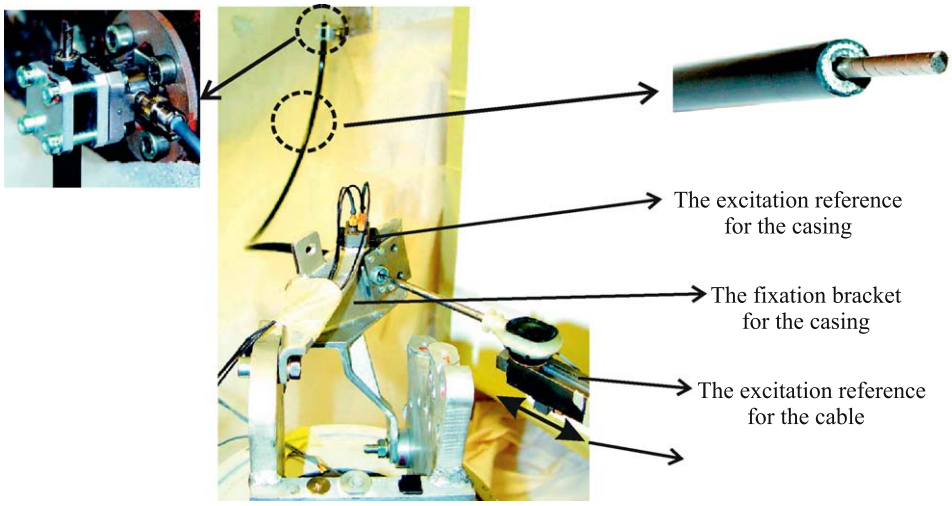

Fig. 18. The experimental set-up for the casing–cable interaction.

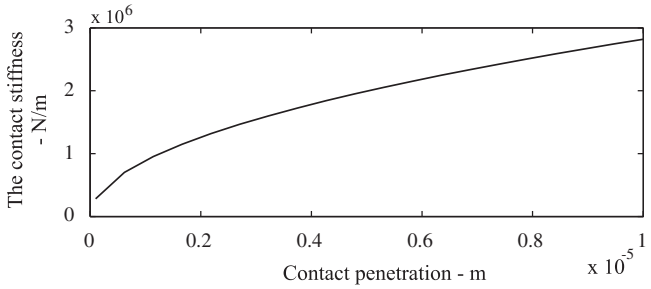

Fig. 19. The relationship between the contact stiffness and the penetration (from the Hertz theory).

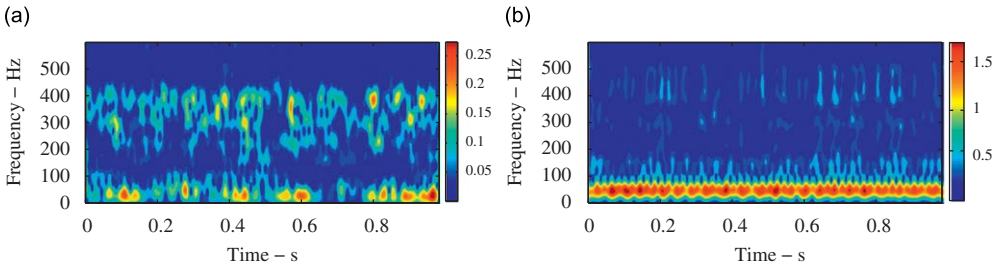

Fig. 20. The wavelet transform of the measured support force in the *z* direction of the cable with casing: (a) with no longitudinal excitation of the cable and (b) with longitudinal excitation of the cable.

Fig. 18. The influence is clearly visible from the wavelet transform of the measured support force in Fig. 20. The peaks in Fig. 20(a) are visible close to the natural frequencies of the casing, while in Fig. 20(b), when we also excite the cable, the higher peaks in the wavelet transform correspond to the frequency of the cable excitation and its harmonics. From this we conclude a very important fact, i.e., for the casing–cable interaction the relative movement of the casing excitation and the cable excitation is very significant.

In the validation process of the mathematical model for the cable with a casing, the numerical model showed a similar indication of the influence of the longitudinal cable's excitation, Fig. 21.

4.3. The contact area

For the optimisation of the casing–cable structure in terms of vibration transmission, the area in the casing–cable system with the highest number of contacts is also of interest. With the used experimental set-up an indication of the

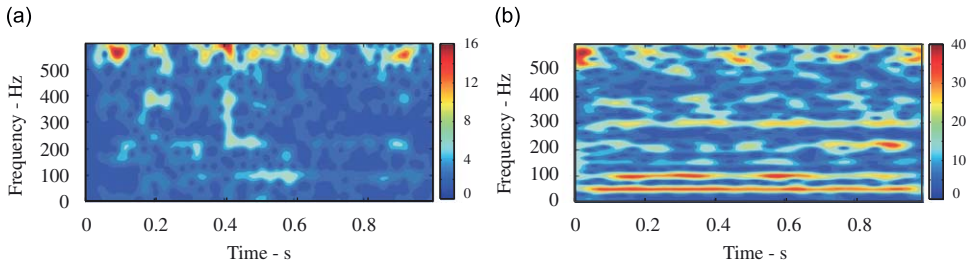

Fig. 21. The wavelet transform of the numerically computed support force in the z direction of the cable with casing: (a) with no longitudinal excitation of the cable and (b) with longitudinal excitation of the cable.

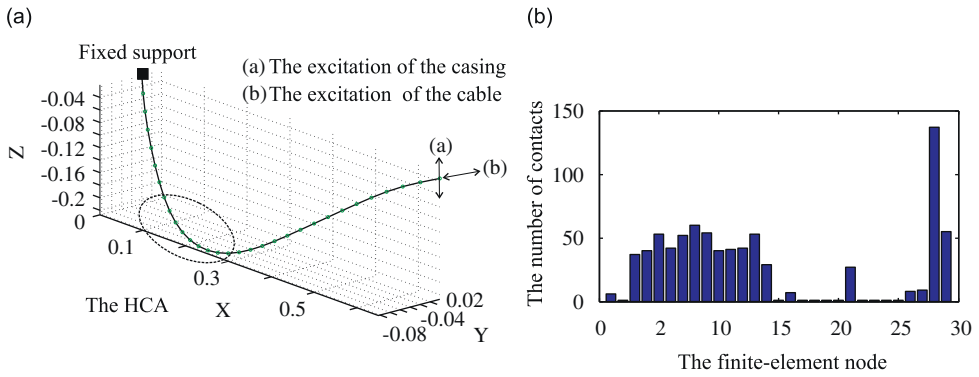

Fig. 22. (a) The HCA area and (b) the HCA histogram for the finite-element nodes.

Table 3
The limit values of the octave bands.

The label for the octave band	1	2	3	4	5	6	7	8	9
f_{lo} (Hz)	11	22	44	88	177	355	710	1420	2840
f_{up} (Hz)	22	44	88	177	355	710	1420	2840	5680

highest contact area (HCA) is not possible, but the numerical casing–cable model gives a good insight into the HCA. For the studied case, the HCA histogram is shown in Fig. 22, and we can see from Fig. 22 that the HCA is in the area of the highest curvature of the cable with casing.

4.4. *The influence of the casing–cable system's properties on the vibration transmission*

The analysis of the influence of the casing–cable system properties is introduced for the purpose of optimising the vibration transmission. The parameters that were analysed are:

1. the dynamic modulus of elasticity of the cable, E_{jv},
2. the dynamic modulus of elasticity of the casing, E_{op},
3. the outer diameter of the cable, D_{zo},
4. the inner diameter of the casing, d_5,
5. the amplitude of the longitudinal excitation of the cable, $\overline{X}_{jv}$,
6. the coefficient of contact friction of the casing–cable interaction, η.

Having accounted for these many parameters, the correlation analysis was made with the Monte Carlo parameter simulation. The most visible output is the force support; therefore, it was chosen to be the objective parameter. The tracked value was the RMS value of the time response of the force support in the z direction.

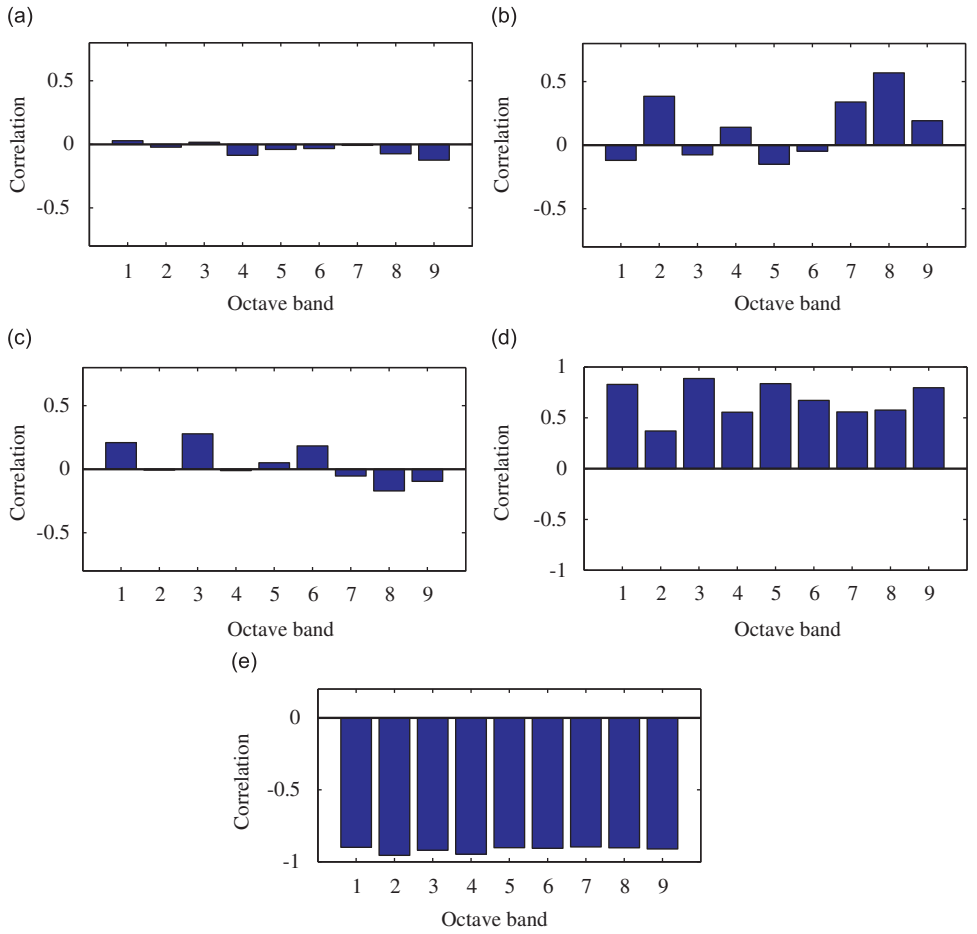

Fig. 23. The correlations between the chosen parameters and the RMS value of the support force in different octave bends: (a) E_{jv}, the dynamical modulus of elasticity of the cable; (b) E_{op}, the dynamical modulus of elasticity of the cable; (c) $gap = d_5 - D_{zo}$, the radial gap between the casing and the cable; (d) $\overline{X}_{jv}$, the amplitude of the longitudinal excitation of the cable; and (e) η, the coefficient of contact friction of the casing–cable interaction.

The study showed that the accounted parameters have different influences in the different frequency bands of interest. Furthermore, the influence analysis was studied in the octave bands from Table 3, where f_{lo} is the lower frequency and f_{up} the upper frequency of the octave band. This gives an insight into the influence of the chosen parameters for a different frequency band. From this the parameter optimisation is made for every operational frequency in the real environment.

Over 300 numerical simulations were made to get the best results for the influence of the chosen parameters. The boundary values for the accounted parameters are: $E_{jv} = 3 \times 10^{10} - 8.5 \times 10^{10}\,\mathrm{N/m^2}$, $E_{op} = 0.2 \times 10^{10} - 1 \times 10^{10}\,\mathrm{N/m^2}$, $D_{zo} = 0.003 - 0.0033\,\mathrm{m}$, $d_5 = 0.0034 - 0.0046\,\mathrm{m}$, and $\eta = 0.05 - 0.2$.

The correlation for the chosen casing–cable parameters to the support force in the z direction is presented in Fig. 23 for different octave bands.

5. Conclusions

This paper presents an analysis of vibration transmission over a spatially curved cable with a casing and with no axial pre-load. The work is an extension of our analysis of cable vibration presented in Ref. [20]. The focus is placed on the vibration modeling of a cable and casing with a gap, the interaction between the casing and the cable and the correlation of the geometrical and the material parameters with the RMS value of the support force, which characterise the vibration transmission.

The casing is modelled as a beam structure on the basis of Euler–Bernoulli beam theory with no axial pre-load. The dissipation of the energy was approximated with two different models of damping, i.e., the viscous damping model and the structural damping model. The results in Fig. 17(a–c) show that the mathematical model is suitable for estimating the casing's natural frequencies. The amplitude of the numerically computed TRFAM is in some frequency regions different from the measured one, but as a whole the comparison is useful. The structural damping model proved to give better results than the viscous damping model. It is clear from Fig. 16 that the consideration of a non-proportional damping model

or the generalised proportional damping of Adhikari [12] would be more appropriate. It should be pointed out that our studies, on the other hand, showed the negligible influence of the small changes in the damping forces on the dynamical system's (cable–casing interaction) time response.

For the modeling of the casing–cable interaction, the frictional contact needs to be addressed in order for the model to show a similar dynamic characteristic to the experiment. The numerical simulation showed that a higher value of the coefficient of friction lowers the vibration transmission for all the observed frequency regions. The correlation also shows the small influence of the dynamic modulus of elasticity of the cable in comparison to the dynamic modulus of elasticity of the casing. The influence of the latter parameter has a tendency to increase the vibration transmissibility at higher frequencies (7th, 8th, 9th octave). It was also shown that the amplitude of the longitudinal excitation of the cable has a significant influence on the increase of the vibration transmissibility. The correlation analysis of the gap value showed that it is frequency dependent. For the 1st and 3rd octave bands it has a tendency to increase the vibration transmissibility and at higher frequencies the bigger gap lowers the vibration transmissibility.

Overall, the mathematical model is suitable for a characterisation of the casing and the casing–cable system's dynamics.

Acknowledgements

The support of D.D. Cimos, Slovenian Research Agency and Ministry of the Economy of the Republic of Slovenia is greatly acknowledged.

References

[1] G.A. Costello, *Theory of Wire Rope*, Springer, Berlin, 1990.
[2] A. Nawrocki, M. Labrosse, A finite element model for simple straight wire rope strands, *Computers & Structures* 77 (2000) 345–359.
[3] N. Barbieri, O.H. de Souza, R. Barbieri, Dynamical analysis of transmission line cables: part 2—damping estimation, *Mechanical Systems and Signal Processing* 18 (2004) 671–681.
[4] N. Barbieri, O.H. de Souza, R. Barbieri, Dynamical analysis of transmission line cables: part 1—linear theory, *Mechanical Systems and Signal Processing* 18 (2004) 659–669.
[5] V. Gattulli, L. Martinelli, F. Perotti, F. Vestroni, Nonlinear oscillations of cables under harmonic loading using analytical and finite element models, *Computer Methods in Applied Mechanics and Engineering* 193 (2004) 69–85.
[6] C.G. Koh, Y. Zhang, S.T. Quek, Low-tension cable dynamics: numerical and experimental studies, *Journal of Engineering Mechanics* March (1999) 347–354.
[7] C.G. Koh, Y. Rong, Dynamic analysis of large displacement cable motion with experimental verification, *Journal of Sound and Vibration* 272 (2004) 187–206.
[8] S. Adhikari, Damping Models for Structural Vibration, Ph.D. Dissertation, Engineering Department, Cambridge University, 2000.
[9] S. Adhikari, J. Woodhouse, Identification of damping: part 1, viscous damping, *Journal of Sound and Vibration* 243 (1) (2001) 43–61.
[10] S. Adhikari, J. Woodhouse, Identification of damping: part 1, non-viscous damping, *Journal of Sound and Vibration* 243 (1) (2001) 63–88.
[11] H.T. Banks, D.J. Inman, On damping mechanisms in beams, *Journal of Applied Mechanics* 58 (3) (1991) 716–723.
[12] S. Adhikari, Damping modelling using generalized proportional damping, *Journal of Sound and Vibration* 293 (1) (2006) 156–170.
[13] J. Woodhouse, Linear damping models for structural vibrations, *Journal of Sound and Vibration* 215 (1998) 547–569.
[14] N.M.M. Maia, J.M.M. Silva, *Theoretical and Experimental Modal Analysis*, Wiley, New York, 1997.
[15] S.S. Rao, *Mechanical Vibrations*, Purdue University, 1995.
[16] G. von Groll, Windmilling in Aero-Engines, Ph.D. Dissertation, Imperial College of Science, Technology & Medicine, University of London, 2000.
[17] G. von Groll, D.J. Ewins, The harmonic balance method with arc-length continuation in rotor/stator contact problems, *Journal of Sound and Vibration* 214 (2001) 223–233.
[18] R.I. Leine, D.H. van Campen, W.J.G. Keultjes, Stick–slip whirl interaction in drillstring dynamics, *Journal of Vibration and Acoustics* 124 (2002) 209–220.
[19] A.S. Yigit, A.P. Christoforou, Coupled torsional and bending vibrations of drillstrings subject to impact with friction, *Journal of Sound and Vibration* 104 (1998) 167–181.
[20] M. Otrin, M. Boltežar, Damped lateral vibrations of straight and curved cables with no axial pre-load, *Journal of Sound and Vibrations* 300 (2007) 676–694.
[21] M. Otrin, M. Boltežar, The vibration over spatially curved steel wire cable with an outer band, *Journal of Mechanical Engineering* 53 (10) (2007) 635–656.
[22] P. Wriggers, *Computational Contact Mechanics*, Wiley, New York, 2002.
[23] H.K. Hong, C.S. Liu, Coulomb friction oscillator: modelling and responses to harmonic loads and base excitations, *Journal of Sound and Vibration* 229 (2000) 1171–1192.
[24] J. Swevers, F. Al-Bender, C.G. Ganseman, T. Prajogo, An integrated friction model structure with improved presliding behavior for accurate friction compensation, *IEEE Transactions on Automatic Control* 45 (4) (2000) 675–686.
[25] C.C. de Wit, H. Olsson, K.J. Aström, P. Lischinsky, A new model for control of systems with friction, *IEEE Transactions on Automatic Control* 40 (3) (1995) 419–425.
[26] C.S. Liu, H.K. Hong, D.Y. Liou, Two-dimensional friction oscillator: group-preserving scheme and handy formulae, *Journal of Sound and Vibration* 266 (2003) 49–74.
[27] B.D. Yang, C.H. Menq, Characterization of 3D contact kinematics and prediction of resonant response of structures having 3D frictional constraint, *Journal of Sound and Vibration* 217 (1998) 909–925.
[28] S.W. Kim, Contact Dynamic and Force Control of Flexible Multi-body Systems, Ph.D. Dissertation, Department of Mechanical Engineering, McGill University, Montreal, Canada, 1999.
[29] J. Perret-Liaudet, E. Rigaud, Response of an impacting Hertzian contact to an order-2 subharmonic excitation: theory and experiments, *Journal of Sound and Vibration* 296 (2006) 319–333.
[30] M. Parssinen, Hertzian contact vibrations under random external excitation and surface roughness, *Journal of Sound and Vibration* 214 (1998) 779–783.
[31] J. Perret-Liaudet, E. Rigaud, Experiments and numerical results on non-linear vibrations of an impacting Hertzian contact. Part 2: random excitation, *Journal of Sound and Vibration* 265 (2003) 309–327.
[32] E. Rigaud, J. Perret-Liaudet, Experiments and numerical results on non-linear vibrations of an impacting Hertzian contact. Part 1: harmonic excitation, *Journal of Sound and Vibration* 265 (2003) 289–307.

[33] I. Chowdhury, S.P. Dasgupta, *Computation of Rayleigh Damping Coefficients for Large Systems*, Department of Civil Engineering, Indian Institute of Technology, India, 1998.
[34] J. Slavič, I. Simonovski, M. Boltežar, Damping identification using a continuous wavelet transform: application to real data, *Journal of Sound and Vibration* 262 (2003) 291–307.
[35] D.J. Ewins, *Modal Testing: Theory and Practise*, Wiley, New York, 1984.
[36] D.J. Henwood, Approximating the hysteretic damping matrix by viscous matrix for modeling in the time domain, *Journal of Sound and Vibration* 254 (2002) 575–593.
[37] M. Otrin, Vibration Characterisation of Steel Wires with Casing, Ph.D. Dissertation, Faculty of Mechanical Engineering, University of Ljubljana, 2008.